Desalination and Water Treatment
www.deswater.com

doi: 10.5004/dwt.2018.21853

109 (2018) 72–89
March

Numerical modeling of an inner preheating transpiring-wall reactor for supercritical water oxidation

Fengming Zhang[a,b,*], Chuangjian Su[a,b], Chunyuan Ma[c]

[a]*Guangzhou Institutes of Advanced Technology, Chinese Academy of Sciences, Guangzhou 511458, China, Tel. +86-020-22912754; Fax: +86-020-22912525; email: fm.zhang@giat.acn.cn (F. Zhang)*
[b]*Shenzhen Institutes of Advanced Technology, Chinese Academy of Sciences, Shenzhen 518055, China, Tel. +86-020-22912607; Fax: +86-020-22912525; email: 273884327@qq.com (C. Su)*
[c]*National Engineering Laboratory for Coal-Fired Pollutants Emission Reduction, Shandong University, Jinan 250061, China, Tel. +86-0531-88399369; Fax: +86-0531-88395877; email: pheres8@mail.sdu.edu.cn*

Received 5 June 2017; Accepted 23 December 2017

ABSTRACT

A computational fluid dynamic model was developed for an inner preheating transpiring-wall reactor for supercritical water oxidation, and the model was validated by analyzing the experimental data. The anticorrosion performance and salt plugging avoidance of the transpiring-wall reactor depended mainly on the water film formation at subcritical temperature on the inner surface of the porous wall. This formation is generally characterized by the porous tube's inner surface temperature, which was determined mainly by the transpiring water temperature (T_{tw1}). Thus, the temperature of the water film formation ($T_{tw1,cr}$) was qualitatively defined as the highest T_{tw1} that can maintain the porous tube's inner surface temperature below 374°C. Furthermore, the interactions between the water film formation and the reaction inside the reactor were investigated. Results indicated that increased values of feed concentration, feed flow rate, mass flow ratio of the feed, and the auxiliary heat source (F_f/F_{au}) were favorable to feed degradation at the same T_{tw1}. However, TOC_{out} and CO significantly increased with increased feed concentration, feed flow rate, and F_f/F_{au} at the corresponding $T_{tw1,cr}$.

Keywords: Supercritical water oxidation; Inner preheating; Transpiring-wall reactor; Computational fluid dynamics; Product properties

1. Introduction

Supercritical water (P > 22.1 MPa and T > 374°C) exhibits its unique thermophysical properties that are absent in water under ambient conditions [1]. Non-polar organic compounds and gases easily dissolve in supercritical water, and a single-phase organic compound–oxygen mixture forms in supercritical water [2,3]. In this unique property, supercritical water is an excellent medium for disposing organic waste. Organic compounds can be fully destroyed at a fast reaction rate with a residence time of a few seconds to 1 min, and no SO_2 and NO_x by-products are formed because of the low reaction temperature (400°C–650°C) [4–6]. Thus, supercritical water oxidation (SCWO) has become a promising technology for disposing organic waste.

Several SCWO-based devices have been designed for industrial applications over the past two decades [7,8]. However, the commercialization of these devices is hindered by technical problems such as corrosion and salt plugging [9]. The plugging problem in the reactor and other pipelines is caused by the precipitation of sticky salts and solids, which occurs because of the poor solubility of inorganic salts in supercritical water, ultimately leading to a system shutdown [10]. Meanwhile, the severe corrosion problems in the entire system, particularly the reactor, result from the combined effects of reactive ions (e.g., Cl^-, F^-, and H_3O^+), high temperature, high pressure, and excessive oxygen [11].

Transpiring-wall reactors have been proven effective in solving both corrosion and salt plugging problems through

* Corresponding author.

fluid dynamic methods [12]. This design contains dual shells, consisting of an outer pressure-resistant vessel and an inner porous tube. A protective water film or at least a flushing effect is formed when low-temperature (<400°C) transpiring water passes through the porous pipe. This transpiring effect prevents solids or precipitated salts from sticking onto the inner surface of the porous tube, thereby improving corrosion resistance. The anticorrosion and salt plugging avoidance performance of the transpiring-wall reactor have been verified and tested by extensive experiments [13].

The feed must be preheated to high temperatures (370°C–500°C) before an SCWO reaction can proceed. However, a coking problem can arise because of the decomposition of organic compounds during the preheating step, resulting in a deteriorated heat transfer or even equipment blockage. Moreover, salt plugging can easily occur if the salt precipitates in the feed [14,15]. This problem can be solved by injecting the reagents at room temperature over a hydrothermal flame and transferring the feed preheating from the exterior to the interior of the reactor [16]. The Swiss Federal Institute of Technology was the first to demonstrate that the feed can be injected into a reactor at room temperature and preheated by a diffusion hydrothermal flame generated by the auxiliary fuel inside a transpiring-wall SCWO reactor [17]. The characteristics of the hydrothermal flame inside the transpiring-wall SCWO reactor have been assessed by Bermejo et al. [18] and Zhang et al. [19].

In our previous work, an inner preheating transpiring-wall reactor was designed based on our previous reactor; the feed was injected into the transpiring-wall reactor at room temperature and preheated by hot water at 550°C with a coaxial nozzle [20]. Although the inner preheating transpiring-wall reactor was successfully operated, an extremely high temperature zone was present below the nozzle because of the formation of the hydrothermal flame; consequently, overheating of the pressure shell and the porous tube was prone to occur [20]. Thus, the reactor performance can be improved by gaining deeper insight into the complex fluid flow, reactions, and heat transfer inside the reactor. However, existing experimental methods can obtain only limited temperature measurements and effluent characterizations because of the extreme reaction conditions inside the reactor.

Computational fluid dynamic (CFD) technique provides an alternative strategy for obtaining comprehensive information that is difficult to measure inside the transpiring-wall reactor. Abeln et al. [21], Bermejo et al. [22], and Zhang and Ma [23] simulated SCWO with a traditional transpiring-wall reactor to elucidate the temperature and species distributions. Lieball [24] performed a CFD simulation of the SCWO of methanol in a transpiring-wall reactor with a hydrothermal flame as an internal heat source. These reports indicated that the reactor structures and the operating parameters significantly influenced the velocity and temperature profiles. Moreover, water film formation was critical to the reactor's anticorrosion and salt plugging avoidance. To date, a proper criterion has yet to be established for water film formation, except for our previous assumption on water film formation that the ideal water film is formed when the inner surface temperature of the porous tube was below 374°C [23]. Xu et al. [25] theoretically analyzed the heat and mass transfer between the water film and the bulk fluid. Nonetheless, the interactions between the water film formation and the reaction inside the reactor remain unclear.

In the present study, an inner preheating transpiring-wall reactor was modeled by commercial CFD software (Fluent 6.3.26) based on our previous experimental data [20]. A desalinated water–methanol mixture was utilized as the artificial wastewater, and hot water was used as the auxiliary heat source for preheating the feed to the reaction temperature. The study presented detailed velocity, temperature, and species profiles for different operating parameters. The data near the inner surface of the porous tube and the outlet of the nozzle were given particular focus. The interactions between the water film formation and the reaction for different operating parameters (such as feed concentration, mass flow ratio of the feed and the auxiliary heat source F_f/F_{au}, and feed flow) were assessed with respect to our previous assumption on water film formation.

2. Experimental setup

Fig. 1 shows the diagram of the inner preheating transpiring-wall reactor, which consisted of five streams leading toward the transpiring-wall reactor. A coaxial nozzle was used for mixing and preheating the reactants inside the reactor to avoid coke formation and salt plugging during the preheating procedure [19,20]. Hot water (400°C–600°C) was utilized as the auxiliary heat source. The auxiliary heat source, the oxygen, and the feed were injected via the inner, annulus, and outer tubes of the coaxial nozzle on the top of the reactor, respectively. The transpiring water (tw) was divided into the upper (tw1) and lower (tw2) branches of transpiring water (tw2) before being injected into the side of the reactor. The auxiliary heat source and tw1 were preheated with electric heaters. The feed, the oxygen, and tw2 were passed through the reactor at room temperature. Detailed information on the transpiring-wall reactor can be found in Table 1 and our previous works [19,20].

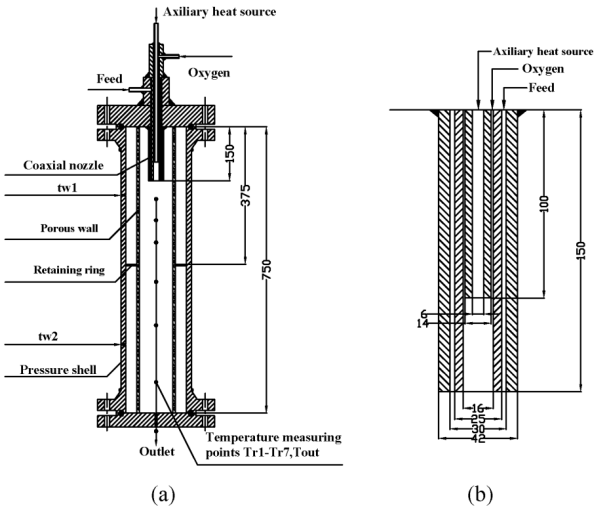

Fig. 1. The schematic diagram of the inner preheating transpiring-wall reactor for supercritical water oxidation (a) and an enlargement of the coaxial nozzle (b).

Table 1
Detailed information of the inner preheating transpiring-wall reactor

Parameter	Value
Reactor geometry	
Material	Steel 321
Diameter of reactor vessel/mm	Φ114 × 17
Length of the reactor/mm	750
Characteristic parameters of the porous tube	
Material	Steel 316L
Diameter of the porous tube/mm	Φ60 × 2.5
Porosity/%	42
Pore size/μm	20.8
Viscosity coefficient/m^2	6.2×10^{-12}
Inertia coefficient/m	3.8×10^{-8}
Nozzle geometry	
Diameter of the inner tube/mm	Φ14 × 4
Length of the inner tube/mm	100
Diameter of the intermediate tube/mm	Φ25 × 4.5
Length of the intermediate tube/mm	150
Diameter of the outer tube/mm	Φ42 × 6
Length of the outer tube/mm	150
Position of the temperature measuring point	
Tr1	H^a = 0.2 m
Tr2	H = 0.25 m
Tr3	H = 0.3 m
Tr4	H = 0.4 m
Tr5	H = 0.5 m
Tr6	H = 0.65 m
T_{out} [b]	H = 0.75 m

[a]H is the distance between the top of the reactor and the temperature measurement point, Tr1–Tr6 are the temperatures of the six measuring points inside the reactor.
[b]T_{out} is the reactor outlet temperature.

The axial temperature distribution was measured by a type K six-point thermocouple (its measuring positions are listed in Table 1) installed inside the reactor. The reactor effluent was cooled and depressurized prior to being introduced into a gas–liquid separator. Then, the gas and liquid phase products were collected and analyzed. The gas effluent was monitored by an online gas analyzer (GASMET FTIR Dx4000), and the liquid samples were collected and analyzed by a total organic carbon analyzer (Shimadzu, TOC 5000A).

3. Model description

3.1. Meshing

The 2D axisymmetric geometry of the reactor was simplified and represented based on its actual size. The pressure shell was not included in the model, because the transpiring water was assumed to be injected uniformly from the inner surface of the pressure shell. Mesh generation was performed with Gambit 2.2.30, and the built mesh contained approximately 115,000 cells. Fig. 2 shows the mesh distribution of the reactor, and the mesh was refined at the nozzle outlet, at which the reaction starts, and on the porous tube's inner surface, where the water film forms.

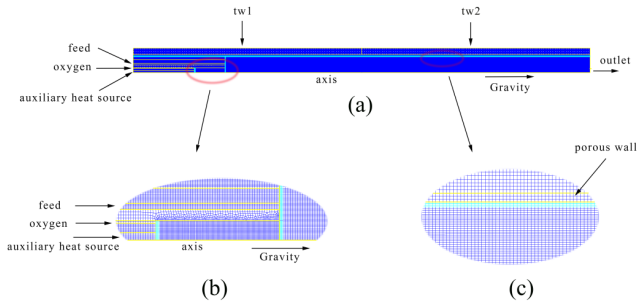

Fig. 2. The mesh of the transpiring-wall reactor for SCWO: (a) the whole reactor, (b) the enlargement of the nozzle outlet, and (c) the enlargement of the inner surface of the porous tube.

3.2. Conservation equations

Governing equations, such as continuity equation, momentum equation, energy equation, turbulence equation, and chemical species equations, were used to describe the complex heat and mass transfer, as well as the reaction process inside the transpiring-wall reactor. All derived quantities were time-averaged quantities obtained by Reynolds averaging of the instantaneous equations in the following governing equations.

The continuity equation for fluid is:

$$\frac{\partial \rho}{\partial t} + \nabla \cdot (\rho \vec{u}) = 0 \tag{1}$$

where ρ is the fluid density, and $\vec{u}$ is the velocity vector.

The momentum equation is described by:

$$\frac{\partial}{\partial t}(\rho \vec{u}) + \nabla \cdot (\rho \vec{u}\vec{u}) = -\nabla p + \nabla \cdot (\bar{\bar{\tau}}) + \rho \vec{g} + \vec{f} \tag{2}$$

where p and $\bar{\bar{\tau}}$ represent the static pressure and the stress tensor, respectively. $\rho\vec{g}$ is the gravitational body force; and $\vec{f}$ is the external body force. The stress tensor $\bar{\bar{\tau}}$ is described by:

$$\bar{\bar{\tau}} = \mu \left[\nabla \vec{u} + \nabla \vec{u}^T - \frac{2}{3}(\nabla \cdot \vec{u}) I \right] \tag{3}$$

where μ is the molecular viscosity, I is the unit tensor, and $\nabla \vec{u}^T$ is the effect of volume dilation.

The effect of heat transfer on hydrodynamics can be calculated by the following energy (E) equation:

$$\frac{\partial}{\partial t}(\rho E) + \nabla \cdot \left[\vec{u}(\rho E + p) \right] = \nabla \cdot \left[k_{eff} \cdot \nabla T - \sum_j h_j \vec{J}_j + (\bar{\bar{\tau}}_{eff} \cdot \vec{u}) \right] + S_h \tag{4}$$

where k_{eff} and T are the effective conductivity and temperature, respectively. $\vec{J}_j$ and h_j represent the diffusion flux and specific enthalpy of species j, respectively. The first three terms on the

right-hand side of Eq. (4) denote the energy transfer due to conduction, species diffusion, and viscous dissipation. The source of energy S_h due to chemical reaction is described by:

$$S_h = -\sum_i \frac{h_i^0}{M_i} r_i \tag{5}$$

where h_i^0, M_i, and r_i are the enthalpy of formation, molar mass, and volumetric creation rate for species *i*, respectively. The species conservation equation is described by:

$$\frac{\partial \rho Y_i}{\partial t} + \nabla \cdot \rho \vec{u} Y_i = -\nabla \cdot D_i \nabla Y_i + r_i, \quad i = 1,...N_{sp} \tag{6}$$

where Y_i, D_i, and r_i are the species mass fraction, mass diffusivity, and production rate of species 'i', respectively. N_{sp} is the number of species. r_i is given by:

$$r_i = \sum_j r_{ij} \tag{7}$$

where r_{ij} represents the production/consumption rate of species *i* in reaction *j*.

3.3. Turbulence model

The renormalization group (RNG) *k*–ε turbulence model is widely used for depicting flow recirculation and vortex shedding scenarios [23,26]. The turbulence kinetic energy *k* and its specific dissipation rate ε in the RNG model can be obtained by using the following equations:

$$\frac{\partial}{\partial t}(\rho k) + \frac{\partial}{\partial x_i}(\rho k u_i) = \frac{\partial}{\partial x_j}(\alpha_k \mu_{eff} \frac{\partial k}{\partial x_j}) + G_k + G_b - \rho\varepsilon - Y_M + S_k \tag{8}$$

$$\frac{\partial}{\partial t}(\rho\varepsilon) + \frac{\partial}{\partial x_i}(\rho\varepsilon u_i) = \frac{\partial}{\partial x_j}(\alpha_\varepsilon \mu_{eff} \frac{\partial \varepsilon}{\partial x_j}) + C_1 \frac{\varepsilon}{k}(G_k + C_3 G_b) - C_2 \rho \frac{\varepsilon^2}{k} - R_\varepsilon + S_\varepsilon \tag{9}$$

$$R_\varepsilon = \frac{C_\mu \eta^3 (1 - \eta/\eta_0)}{1 + \beta\eta^3} \frac{\varepsilon^2}{k} \tag{10}$$

$$\eta = \frac{S_k}{\varepsilon} \tag{11}$$

An RNG *k*–ε model with default values and standard wall functions was used in these equations. G_k represents the turbulence kinetic energy generation due to the mean velocity gradients. G_b represents the turbulence kinetic energy generation due to buoyancy. Y_M represents the change in the overall dissipation rate due to the fluctuating dilatation in the compressible turbulence. S_k and S_ε are the source terms defined by the user. *S* is the modulus of the strain tensor rate. α_k and α_ε are the inverse effective Prandtl numbers for *k* and ε, respectively. $C_1 = 1.42$, $C_2 = 1.68$, $\eta_0 = 4.38$, $\beta = 0.012$, $C_\mu = 0.0845$, and $\alpha_k = \alpha_\varepsilon = 1.39$.

3.4. Kinetic model

The transpiring water is typically injected into the reactor at low temperatures (<400°C). In addition, an Arrhenius-type reaction kinetic equation is generally used for simulation [22,27] to accurately adapt the temperature gradient in the axial and radial temperature profiles of the reactor. Our previous experimental results [19,20] have proven that CO is a major intermediate during the SCWO of methanol inside the transpiring-wall reactor. Thus, a two-step mechanism was designed and implemented in our present model.

$$CH_3OH + O_2 = CO + 2H_2O \tag{12}$$

$$CO + 0.5O_2 = CO_2 \tag{13}$$

The kinetic data used in the present study was based on the literature [28–31], and the reaction order of oxygen was assumed equal to zero because the oxygen is in large excess.

$$r_{CH_4O} = -\frac{d[CH_3OH]}{dt} = 2.0\times10^{21} \times \exp\left(\frac{-326.6}{RT}\right)[CH_3OH] \tag{14}$$

$$r_{CO} = -\frac{d[CO]}{dt} = 3.16\times10^{6} \times \exp\left(\frac{-112}{RT}\right)[CO] \tag{15}$$

3.5. Physical properties

Significant changes were observed in the thermophysical properties of the water near the critical point [1] (Fig. S1 in supplementary material). The sharp curve at the critical point typically results in computational instability, indicating the urgent need for a simplified and suitable model for calculating the physical properties. The Peng-Robinson equation [22,32] implemented by a fluent user defined function was used to approximately calculate the densities of pure species.

$$P = \frac{RT}{(v - b_c)} - \frac{a_c \alpha}{v(v + b_c) + b_c(v - b_c)} \tag{16}$$

$$a_c = 0.45724 \frac{R^2 T_c^2}{P_c^2}; \quad b_c = 0.077796 \frac{RT_c}{P_c} \tag{17}$$

$$\alpha = \left[1 + \kappa(1 - \sqrt{T_r})\right]^2 \tag{18}$$

$$\kappa = 0.37464 + 1.54226\psi - 0.26992\psi^2 \tag{19}$$

where *v* represents the molar volume of the species; P_c and T_c represent the critical pressure and the critical temperature, respectively; *R* represents the universal gas constant; and T_r is calculated by dividing the temperature by the critical temperature. κ and ψ represent the constant characteristic of the component and the acentric factor, respectively.

An approximate heat capacity curve of the water (Fig. S2) was imported to avoid numerical instabilities [33]. Other thermophysical properties (such as viscosity and thermal conductivity) were obtained from the NIST database [34].

The mixture was assumed to be an ideal mixing, such that the mixture properties can be calculated by mass averaging method.

3.6. Porous media

The porous media can be modeled by adding of a momentum source to the standard fluid flow equations. The momentum source can be described by:

$$S_i = -\left(\frac{\mu}{\alpha}u_i + \frac{1}{2}\beta\rho|u|u_i\right) \tag{20}$$

where S_i, which consists of a viscous loss term and an inertial loss term, is the source term for the ith momentum equation; $|u|$ is the velocity magnitude; $1/\alpha$ is viscous coefficient; and β is the inertial coefficient. Darcy's law can be used to describe the flow of the supercritical water in the porous tube [17,35]. Compared with the operating pressure (>22.1 MPa), the decreased pressure across the porous wall was negligible, and the pressure-induced changes in physical properties were generally minimal.

Only modifications of the conduction flux and the transient terms were considered in solving the energy transport equation in the porous tube. The energy transport equation can be expressed as:

$$\begin{aligned}&\frac{\partial}{\partial t}\left[\chi\rho_f E_f + (1-\chi)\rho_s E_s\right] + \nabla\cdot\left[\vec{u}(\rho_f E_f + p)\right] \\ &= \nabla\cdot\left[k_{eff}\nabla T - \left(\sum_i h_i J_i\right) + \left(\bar{\bar{\tau}}\cdot\vec{u}\right)\right] + S_f^h\end{aligned} \tag{21}$$

where E_f and E_s represent the total fluid energy and the total solid medium energy, respectively. χ and k_{eff} denote the porosity of the medium and the effective thermal conductivity, respectively. S_f^h is the source term for fluid enthalpy. k_{eff} is the effective thermal conductivity, which can be computed as:

$$k_{eff} = \chi k_f + (1-\chi)k_s \tag{22}$$

where k_f and k_s refer to the fluid conductivity and the solid conductivity, respectively.

3.7. Numerical methodology

In the reactor simulation, mass-flow-inlet boundary conditions were applied for oxygen, feed, tw1, and tw2; outlet pressure boundary condition was used for the reactor outlet; axisymmetric boundary condition was implemented for the reactor axis; and porous zone condition was utilized for the porous tube.

The conversation equations were numerically solved by the commercial software Fluent 6.3.26 through a finite volume method. Pressure velocity coupling was achieved by using the SIMPLE algorithm. The simulation was started from an initial value, and the solution converged when the residuals became less than certain thresholds. Detailed information of the numerical model is provided in Table 2.

Table 2
Parameter settings and operating conditions in the simulation

Parameter	Value
Boundary condition	
Feed	Mass flow inlet
Oxygen	Mass flow inlet
Auxiliary heat source	Mass flow inlet
tw1	Mass flow inlet
tw2	Mass flow inlet
Outlet	Pressure outlet
Axis	Axisymmetric
Solution	
Algorithm	SIMPLE
Scheme	First-order schemes
Convergence criterion	
Continuity	10^{-4}
Velocity components	10^{-4}
Energy	10^{-7}
k	10^{-5}
E	10^{-5}
Component	10^{-4}

4. Results and discussion

4.1. Parameter definition

The transpiring water flow was determined by the transpiring flow relation R_{tw}, which is defined in Eq. (23). The transpiring flow relations for tw1 and tw2 were assigned with the same values.

$$R_{tw} = \frac{F_{twi}}{F_{au} + F_{ox} + F_f}, \quad i = 1,2 \tag{23}$$

where F_{tw1}, F_{tw2}, F_{au}, F_{ox}, and F_f denote the mass flow rates of the tw1, the tw2, the auxiliary heat source, oxygen, and the feed, respectively. Feed degradation occurred mainly in the supercritical temperature zone, because the reaction rate was considerably faster at the supercritical than at the subcritical temperature zone [20]. The useful length (L_{sup}) was defined as the length of the reactor under supercritical temperatures (>374°C) and was calculated based on the temperature profiles inside the reactor. Similarly, the useful reaction time (t_r) was defined as the residence time of the reactants under supercritical temperatures and was calculated based on the piecewise average flow rates and densities of the reactants, and the calculation method is the same as the previous work using experimental data [20].

4.2. Model validation

Fig. 3 shows a comparison of the experimental and simulated temperature profiles at different F_f/F_{au}. The CFD model underestimated the reaction zone temperatures in the upper part of the reactor (H = 0.15–0.3 m) by 20°C–120°C. For example, Tr1 and Tr2 were 639°C and 553°C, respectively, when F_f/F_{au} = 0.3, whereas the corresponding simulated

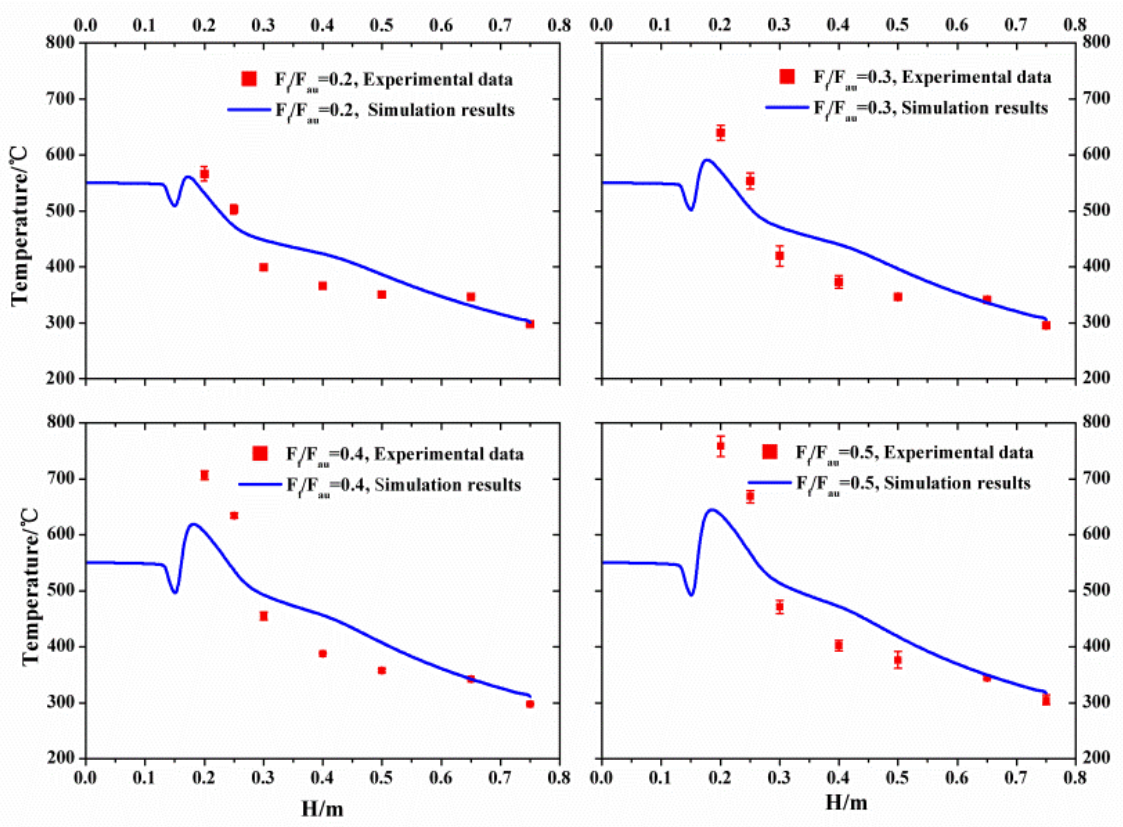

Fig. 3. The experimental and simulated temperature profiles comparisons at different F_f/F_{au}, simulation conditions (integral values of the experimental conditions): F_{au} = 9.5 kg/h, ω_f = 35 wt%, γ = 1.5, $F_{tw1} = F_{tw2}$ = 18 kg/h, T_{au} = 550°C, and T_{tw1} = 350°C.

temperatures were 576°C and 503°C, respectively. These findings indicated that the reaction occurred at or near the hydrothermal flame region at high reaction temperatures in the range of 500°C–800°C [16,18]. The experimental reaction rate was faster than that simulated by the finite rate model [16,23]. A greater reaction heat was released in the experiment than in the simulation, resulting in the higher temperature distributions in this zone. The CFD model overestimated the temperature in the middle part of the reactor (H = 0.30–0.50 m) by 10°C–15°C; the higher predicted temperatures may be due to the simplified water heat capacity and two-phase flow [36] in this zone. For the lower part of the reactor (H = 0.50–0.75 m), the simulation results agreed well with the experimental data.

The calculated and experimental species concentrations at the reactor outlet were compared with further verify the numerical model, and the data are presented in Fig. 4. The reactor effluent consisted of CH_4O, O_2, CO, CO_2, and H_2O. An ideal gas–liquid separation was assumed for the reactor effluent (Fig. S3). Thus, O_2, CO, and CO_2 existed in the gaseous effluent, whereas CH_4O and H_2O existed in the aqueous effluent in the simulation [37]. The incompletely degraded products (TOC_{out} and CO) were compared with the experimental data for model validation. TOC_{out} in the aqueous effluent and CO in the gaseous effluent can be calculated by Eqs. (24) and (25), respectively.

$$TOC_{out} = 10^6 \times \omega_{CH_4O} \times \omega_c \tag{24}$$

$$\varphi_{CO} = \frac{\omega_{CO} / M_{CO}}{\omega_{CO} / M_{CO} + \omega_{CO_2} / M_{CO_2} + \omega_{O_2} / M_{O_2}} \tag{25}$$

where $\omega_{CH_4O}, \omega_{CO}, \omega_{CO_2}, \omega_{O_2}$ denote the mass fractions of CH_4O, CO, CO_2, and O_2 in the effluent, respectively, and ω_c is the mass fraction of carbon in methanol. Although both TOC_{out} and CO markedly changed when F_f/F_{au} was increased in the simulation, the trend and magnitude of TOC_{out} and CO generally agreed with the experimental data for trace values of TOC and CO in the effluent.

Similar conclusions were drawn when the experimental and simulated results were compared at different auxiliary heat source flows, as demonstrated in the supplementary material (Figs. S4 and S5).

4.3. Flow field distribution

$$F_{ox} = 1.5\gamma F_f \omega_f \tag{26}$$

Figs. 5 and 6 show the flow field distributions of the reactor under typical operating conditions (F_f/F_{au} = 0.4, F_{au} = 10 kg/h, T_{au} = 550°C, ω_f = 30 wt%, γ = 1.5, T_{tw1} = 300°C, and R_{tw} = 1.2). F_f/F_{au}, which is a critical parameter for hydrothermal flame ignition, is defined as the ratio of F_f to F_{au} at

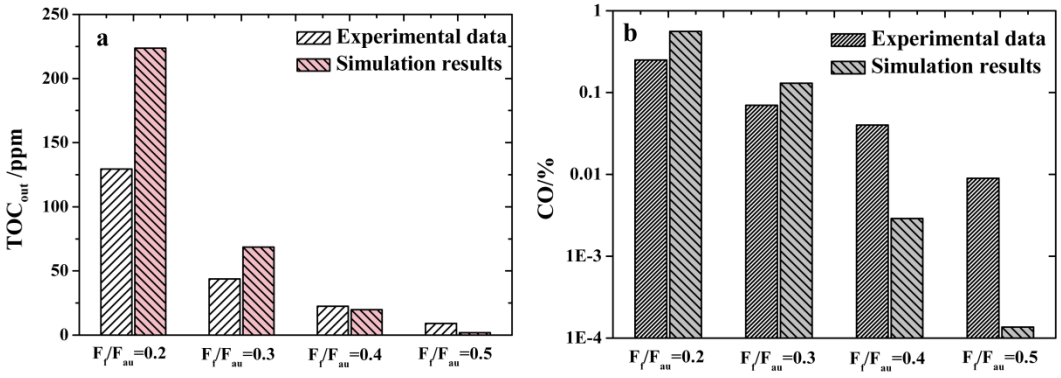

Fig. 4. Comparisons of the experimental and simulated species concentrations of the reactor effluent at different F_f/F_{au} (a) TOC_{out} and (b) CO.

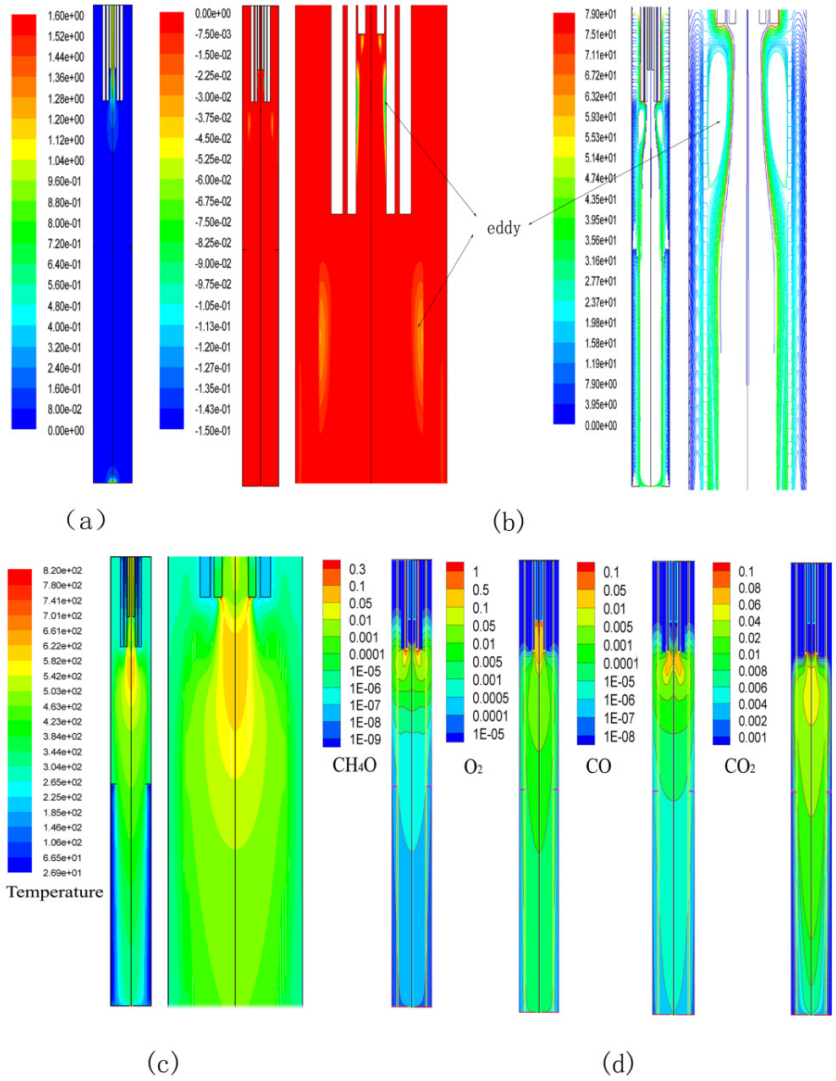

Fig. 5. The whole velocity contours (m/s) (a); axial velocity contours of the whole reactor and the upper part of the reactor with only negative values displaying and path lines characterized by residence time (s) of the whole reactor and the upper part of the reactor (b); simulated temperature contours (°C) of the whole reactor and the upper part of the reactor (c); and species contours of CH_4O, O_2, CO, and CO_2 (d).

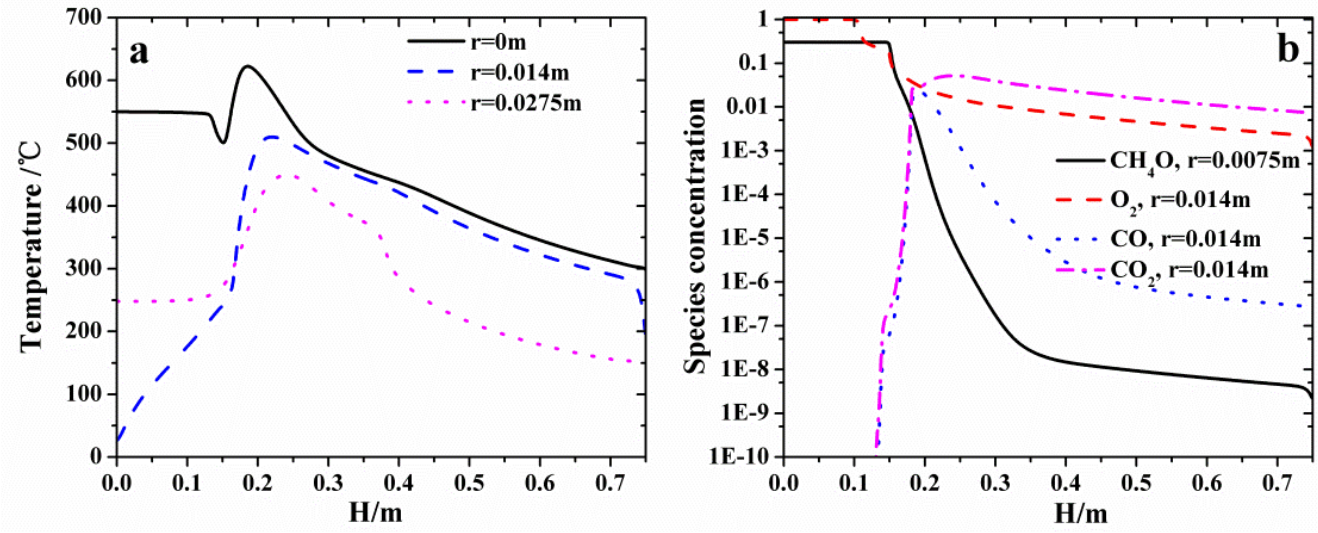

Fig. 6. Temperature and species profiles along the axial direction (*r*: distance from the axis): (a) temperature profiles and (b) species profiles.

constant F_{au} [20]. F_{ox} can be calculated from the stoichiometric oxygen excess (γ) in Eq. (26). The velocity contours (Fig. 5(a)) revealed that the higher velocities were mainly located at the outlet of the nozzle. The entire negative axial velocity contour and the enlarged negative axial velocity contour of the upper part of the reactor are presented in Fig. 5(b, left). The negative axial velocities (countercurrent up) suggested that the eddy phenomenon was caused by jet entrainment. The eddy in the nozzle mixing zone indicated that the hot water mixed with oxygen, whereas the eddy at the nozzle outlet implied that the hot water mixed with the feed. The path line of the entire reactor and the upper part of the reactor (characteristics are highlighted by color) are shown in Fig. 5(b, right); the data also indicates the presence of an eddy phenomenon. A strong mixing occurred in the upper part of the reactor, as proven by the velocity contours (Fig. 5(a)) and path line (Fig. 5(b)). However, a uniform velocity was observed in the middle and lower parts of the reactor.

Fig. 5(d) presents the species contours inside the reactor, and Fig. 6(b) shows the species profiles along the axial direction. The feed entered the reactor and then reacted with the oxygen in the axial nozzle. The methanol and O_2 concentrations rapidly decreased from 0.3 to 10^{-7} and from 1 to 0.01, respectively, at 0–0.2 m below the nozzle outlet, implying that methanol reacted at a fast rate. By contrast, the concentrations of the intermediate product CO and the terminal product CO_2 located below the nozzle outlet rapidly increased. The methanol and CO concentrations in the porous tube reached 10^{-4} and 10^{-5}, respectively; such conditions are not conducive for the complete degradation of the feed at low temperatures.

In addition, the temperature contours (Fig. 5(c)) revealed that methanol had a fast reaction rate at the nozzle outlet; this finding agreed with the species contours. The high-temperature profiles were concentrated at the nozzle outlet (0–100 mm). The hot water (550°C under this condition) at the center of the axial nozzle formed a jet entrainment, which preheated the feed and oxygen at room temperature. As shown in Fig. 6(a), the central temperature initially declined because the heat was transferring from the hot water to the feed and oxygen. The temperature then increased as heat was released during methanol oxidation. The axial temperature gradually declined when the transpiring water was injected at low temperatures. Finally, the bulk flow was cooled to a subcritical temperature before it left the reactor. The temperature difference between the reactor center and the inner surface of the porous tube (r = 0.0275 m) was only 60°C in the upper part of the reactor; the small difference was due to the jet entrainment effect of the reactive fluid, suggesting a continuously stirred tank reactor was probably formed in that part [38]. By contrast, the radial temperature difference was significant and maintained at nearly 200°C in the lower parts of the reactor, implying a plug flow reactor probably existed in those parts.

4.4. Water film formation

When the pressure of the reactor was maintained at 23 MPa, water polarity depended mainly on the temperature [1], and the solubility of the inorganic salt significantly increased when the water temperature became lower than 374°C. Given that water film formation was determined mainly by the temperature on the inner surface of the porous tube inside the transpiring-wall reactor, the ideal water film was assumed to form when the temperature was below 374°C. Such an assumption provided a qualitative method for characterizing the water film. This section focuses on the key parameters of water film formation.

4.4.1. Transpiring flow relation

Figs. 7(a) and (b) show that the temperatures of the reactor center temperature and the inner surface of the porous tube slightly decreased as the transpiring flow relation increased. Higher transpiring flow relations correspond to higher transpiring flow rates, which in turn provide higher

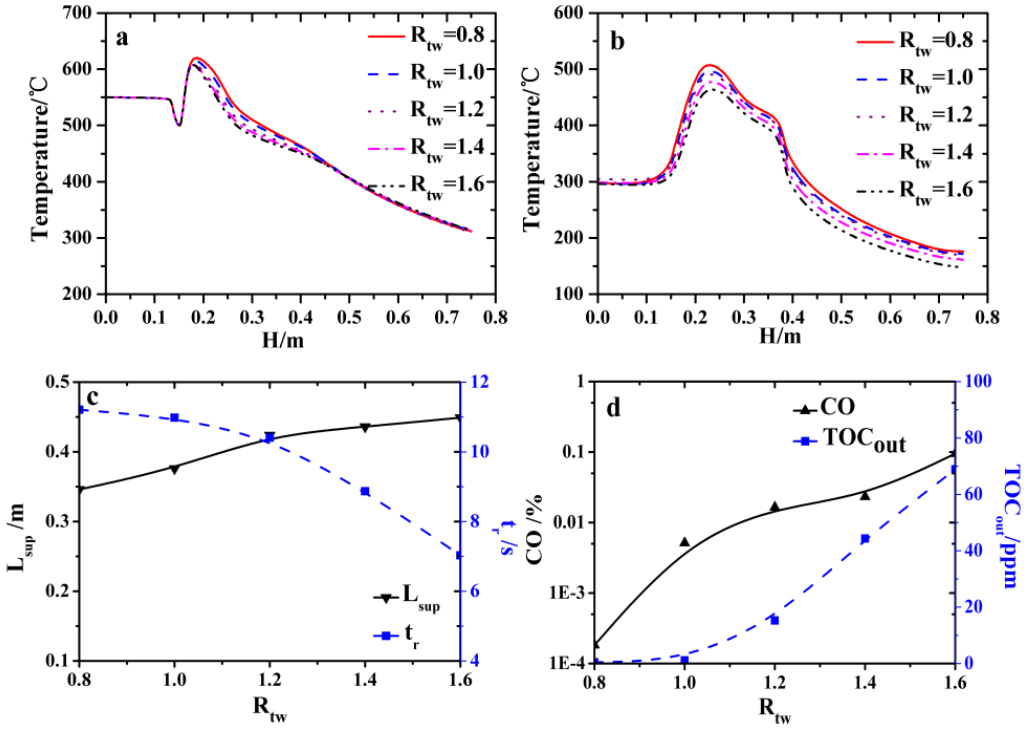

Fig. 7. The effect of transpiring flow relation on temperature profiles and product properties, operating conditions: F_f/F_{au} = 0.4, F_{au} = 10 kg/h, ω_f = 30 wt%, γ = 1.5, T_{tw1} = 300°C, and T_f = 550°C. (a) The axial temperature profiles along the reactor center, (b) the axial temperature profiles along the inner surface of the porous tube, (c) L_{sup} and t_r, and (d) TOC_{out} and CO.

flushing velocities and more cold energy for cooling the reactive fluid. Nonetheless, the transpiring flow relation exerted an insignificant effect on the temperature contours (Fig. S6). The temperature of the inner surface of the porous tube decreased by only 60°C when the transpiring flow relation increased from 0.8 to 1.6 (as the total transpiring flow increased from 26.72 to 53.44 kg/h). The probable reason is that the heat transfer between the transpiring water and the reactive hot fluid was enhanced at higher transpiring intensities.

Higher transpiring flow relations lead to lower useful residence times (Fig. 7(c)). Both TOC_{out} and CO gradually increased as the transpiration intensity was increased (Fig. 7(d)). TOC_{out} and CO were 0.4 ppm and 0.0002% at a transpiring flow relation of 0.8. TOC_{out} and CO increased to 68.9 ppm and 0.0951% when the transpiration intensity was increased to 1.6.

4.4.2. Transpiring water temperature

The analysis of the transpiring water temperature was focused only on the temperature of tw1 (T_{tw1}), because tw2 was at room temperature. The temperatures of both the reaction zone and the inner surface of the porous tube decreased significantly when T_{tw1} was decreased from 300°C to 50°C, indicating that an intense heat transfer occurred between the transpiring water and the reactive fluid (Figs. 8(a) and (b)). Detailed information on the temperature contours are provided in Fig. S7. The highest temperature of the porous wall decreased from 468°C to 295°C when T_{tw1} was decreased from 300°C to 50°C.

T_{tw1} is critical to the inner surface temperature of the porous tube. Thus, the temperature of the water film formation ($T_{tw1,cr}$) was designated as the highest T_{tw1} that can maintain the porous tube's inner surface temperature below 374°C. $T_{tw1,cr}$ was obtained by decreasing T_{tw1} step by step until all inner surface temperatures of the porous wall were below 374°C.

Both L_{sup} and t_r decreased significantly when the cooling effect was enhanced at low T_{tw1}. As shown in Fig. 8(c), L_{sup} rapidly decreased from 0.424 to 0.129 m when T_{tw1} was decreased from 300°C to 50°C, and t_r decreased from 10.41 to 4.84 s. These findings indicated that low T_{tw1} were not conducive for feed degradation, as confirmed by the product properties. Fig. 8(d) shows that the concentrations of both TOC_{out} and CO demonstrated a significant upward trend when the T_{tw1} was decreased. The TOC_{out} concentration of less than 20 ppm at T_{tw1} of 300°C rapidly increased to 212.0 ppm when T_{tw1} was decreased to 50°C. In addition, the concentration of CO increased at an exponential rate as the T_{tw1} was decreased. The CO concentration of less than 0.01% at above 250°C increased to 0.942% and 2.10% at T_{tw1} of 100°C and 50°C, respectively.

4.5. The effect of the operating parameters

The effects of the key operating parameters (such as feed concentration, feed flow, and F_f/F_{au}) on the temperature contours and the product properties are discussed in this section. In addition, the interaction between the water film formation and the reaction for different operating parameters was highlighted.

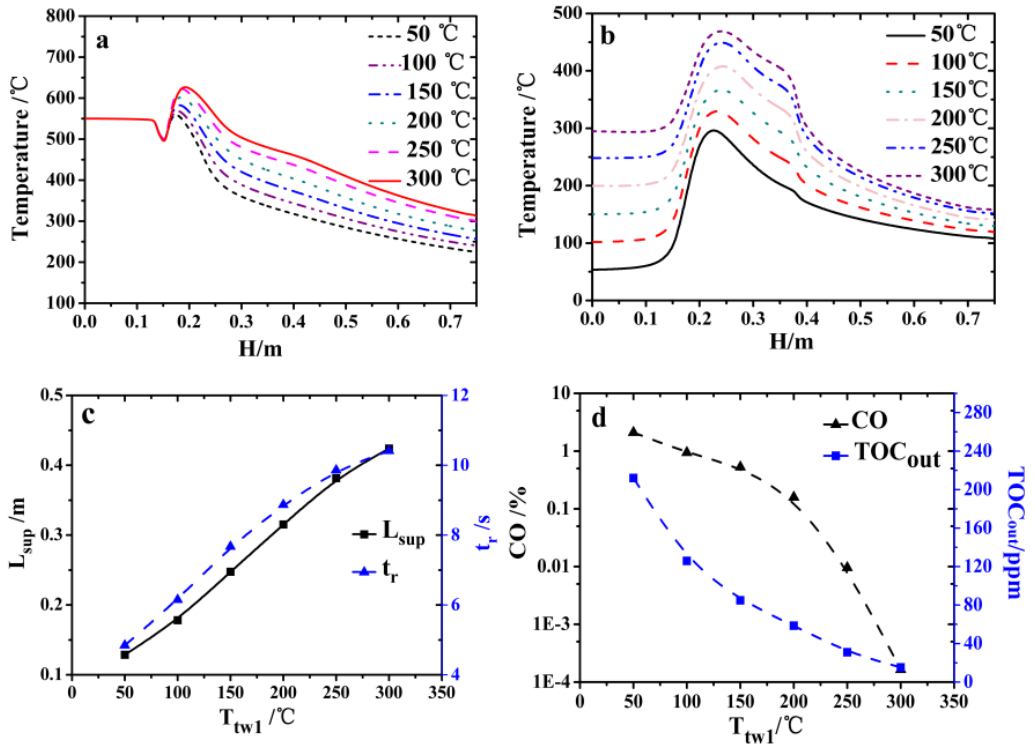

Fig. 8. The effect of T_{tw1} on temperature profiles and product properties, operating conditions: F_f/F_{au} = 0.4, F_{au} = 10 kg/h, ω_f = 30 wt%, T_f = 550°C, and R_{tw} = 1.2. (a) The axial temperature profiles along the reactor center, (b) the axial temperature profiles along the inner surface of the porous tube, (c) L_{sup} and t_r, and (d) TOC_{out} and CO.

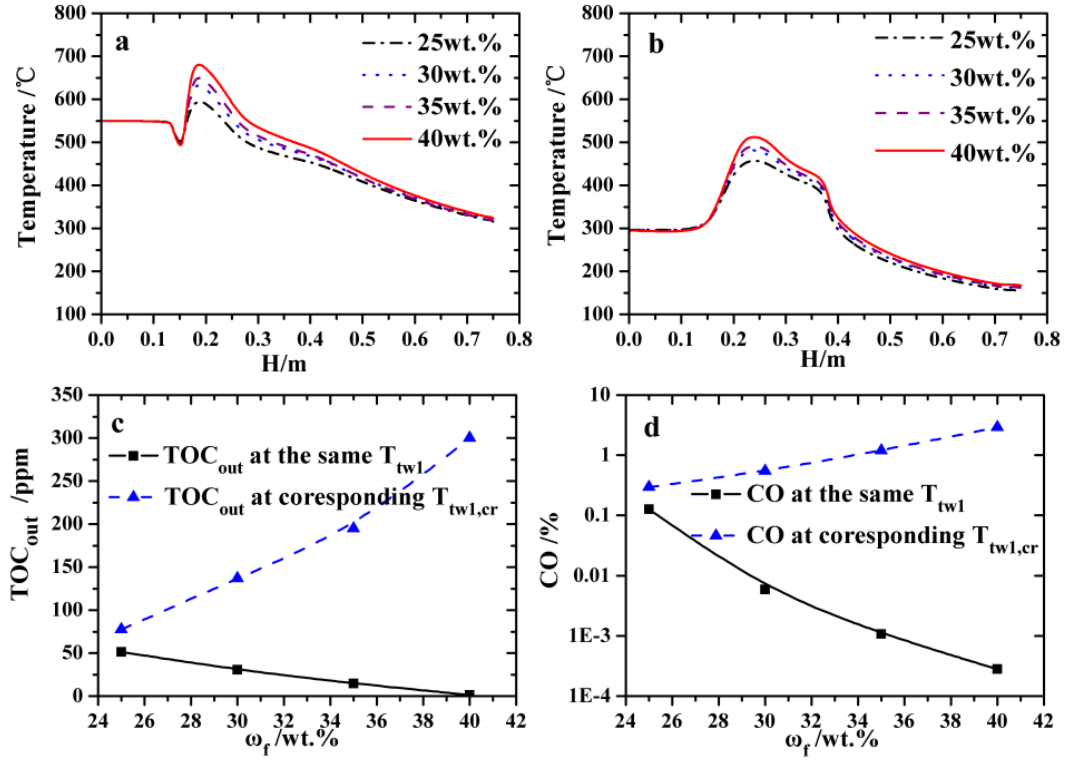

Fig. 9. The effect of feed concentration on temperature profiles and product properties. (a) The axial temperature profiles along the reactor center, (b) the axial temperature profiles along the inner surface of the porous tube, (c) TOC_{out}, and (d) CO.

Table 3
Critical parameters for water film formation at different conditions

No.	F_{au} (kg/h)	F_f (kg/h)	F_f/F_{au}	ω_f (wt%)	γ	R	T_{au} (°C)	$T_{tw1,cr}$ (°C)	L_{sup} (m)	t_r (s)
A1	9.0	4.0	0.44	25	1.5	1.2	550	198.1	0.364	8.43
A2	9.0	4.0	0.44	30	1.5	1.2	550	173.0	0.346	7.84
A3	9.0	4.0	0.44	35	1.5	1.2	550	148.6	0.331	7.01
A4	9.0	4.0	0.44	40	1.5	1.2	550	125.9	0.319	6.18
B1	10.0	2	0.2	30	1.5	1.2	550	182.5	0.361	6.88
B2	10.0	3	0.3	30	1.5	1.2	550	148.5	0.358	6.46
B3	10.0	4	0.4	30	1.5	1.2	550	118.3	0.351	6.18
B4	10.0	5	0.5	30	1.5	1.2	550	90.0	0.347	5.97
C1	6.0	2.4	0.4	35	1.5	1.2	550	184.0	0.387	14.31
C2	8.0	3.2	0.4	35	1.5	1.2	550	148.9	0.372	10.07
C3	10.0	4.0	0.4	35	1.5	1.2	550	117.2	0.368	7.46
C4	12.0	4.8	0.4	35	1.5	1.2	550	85.1	0.358	5.94
C5	14.0	5.6	0.4	35	1.5	1.2	550	54.0	0.350	4.61

4.5.1. Feed concentration

Figs. 9(a) and (b) show the temperature profiles of the reactor center and the inner surface of the porous tube under the operating conditions listed in Table 3 (A1–A4). The reaction temperature rapidly increased as the feed concentration was increased. The reaction temperatures were 594°C, 621°C, 659°C, and 689°C at feed concentrations of 25, 30, 35, and 40 wt%, respectively. In addition, the inner surface temperature of the porous tube increased correspondingly, and the highest temperature increase was from 456°C to 512°C when the feed concentration was increased from 25 to 40 wt%.

To investigate the interactions between the water film formation and the reaction, we first obtained the values of $T_{tw1,cr}$ and the other parameters for the ideal water film formation at different feed concentrations (Table 3, A1–A4). When the feed concentration was 25 wt%, $T_{tw1,cr}$ was 198.1°C, which then decreased to 125.9°C when the feed concentration was 40 wt%. The decrease in the T_{tw1} decreased not only the inner surface temperature of the porous wall for water film formation but also the temperature of the reactor, thus reducing L_{sup} and t_r.

Figs. 9(c) and (d) show comparisons of TOC_{out} and CO as functions of feed concentration at the same T_{tw1} of 300°C and the corresponding $T_{tw1,cr}$, respectively. The concentrations of TOC_{out} and CO decreased from 51.4 to 1.3 ppm and from 0.17% to 0.0003%, respectively, when the feed concentration was increased from 25 to 40 wt% at the same T_{tw1}. By contrast, in the presence of a water film at the corresponding $T_{tw1,cr}$, the concentrations of TOC_{out} and CO were 77.6 ppm and 0.295%, respectively, at a feed concentration of 25 wt%, and these values rapidly increased to 299.8 ppm and 2.912%, respectively, when the feed concentration was increased to 40 wt% (Figs. 9(c) and (d)). These findings indicated that feed degradation was further retarded at higher feed concentrations when a water film was formed. A feed concentration of less than 30% was determined for this reactor.

4.5.2. F_f/F_{au}

Although a higher F_f/F_{au} corresponded to a lower nozzle outlet temperature, the concentration of methanol at the nozzle outlet increased as F_f/F_{au} was increased at a constant flow rate of auxiliary heat source [19]. Thus, the temperatures of the reactor center and the inner surface of the porous tube increased significantly when F_f/F_{au} was increased (Figs. 10(a) and (b)). The reaction temperature increased linearly when F_f/F_{au} was increased. The reaction temperatures were 557°C, 588°C, 615°C, and 639°C at F_f/F_{au} of 0.2, 0.3, 0.4, and 0.5, respectively, and the corresponding highest temperatures of the inner surface of the porous wall were 448°C, 468°C, 487°C, and 504°C.

We first obtained the values of $T_{tw1,cr}$ and the other parameters for the ideal water film formation at different F_f/F_{au} (Table 3, B1–B4). $T_{tw1,cr}$ was 182.5°C at F_f/F_{au} of 0.2, which decreased to 90°C when F_f/F_{au} was increased to 0.5. The decrease in the T_{tw1} also decreased the temperature of the reactor, thus reducing L_{sup} and t_r (Table 3, B1–B4).

Figs. 10(c) and (d) show comparisons of TOC_{out} and CO as functions of F_f/F_{au} at the same T_{tw1} of 300°C and the corresponding $T_{tw1,cr}$, respectively. TOC_{out} and CO decreased from 123.6 to 3.9 ppm and from 0.2656% to 0.0004%, respectively, when F_f/F_{au} was increased from 0.2 to 0.5 at the same T_{tw1}. The decrease in $T_{tw1,cr}$ retarded the feed degradation, particularly at high F_f/F_{au}. At the corresponding $T_{tw1,cr}$ for water film formation, when F_f/F_{au} was 0.2, TOC_{out} and CO were 158.3 ppm and 0.567%, respectively, which rapidly increased to 346.9 ppm and 2.569% when F_f/F_{au} was 0.5. Thus, an F_f/F_{au} of less than 0.3 was considered appropriate for this reactor.

4.5.3. Feed flow

Higher feed flows resulted in higher temperature profiles of the reactor center and the inner surface of the porous wall, as shown in Figs. 11(a) and (b). $T_{tw1,cr}$ was 184.0°C at a feed flow of 2.4 kg/h, which decreased to 54.0°C when the feed flow was increased to 5.6 kg/h. The decrease in the transpiring water temperature also decreased the temperature of the reactor, thereby reducing L_{sup} and t_r (Table 3, C1–C5).

Figs. 11(c) and (d) show comparisons of TOC_{out} and CO as functions of feed flow at the same T_{tw1} of 300°C and the corresponding $T_{tw1,cr}$, respectively. TOC_{out} and CO slightly

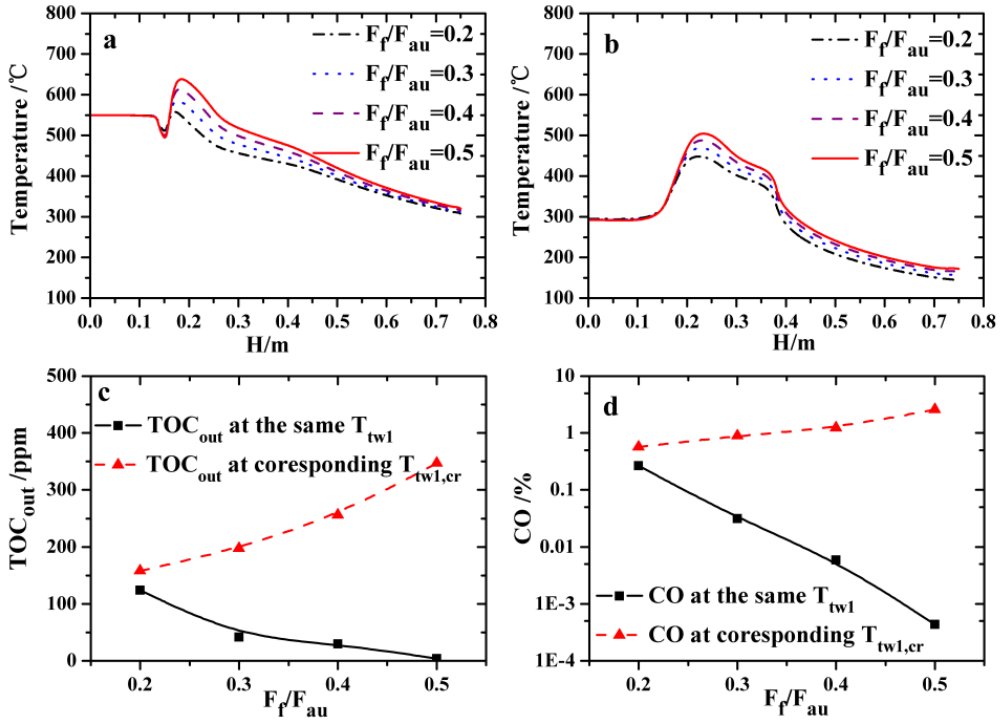

Fig. 10. The effect of F_f/F_{au} on temperature profiles and product properties. (a) The axial temperature profiles along the reactor center, (b) the axial temperature profiles along the inner surface of the porous tube, (c) the concentration of TOC_{out}, and (d) the concentration of CO.

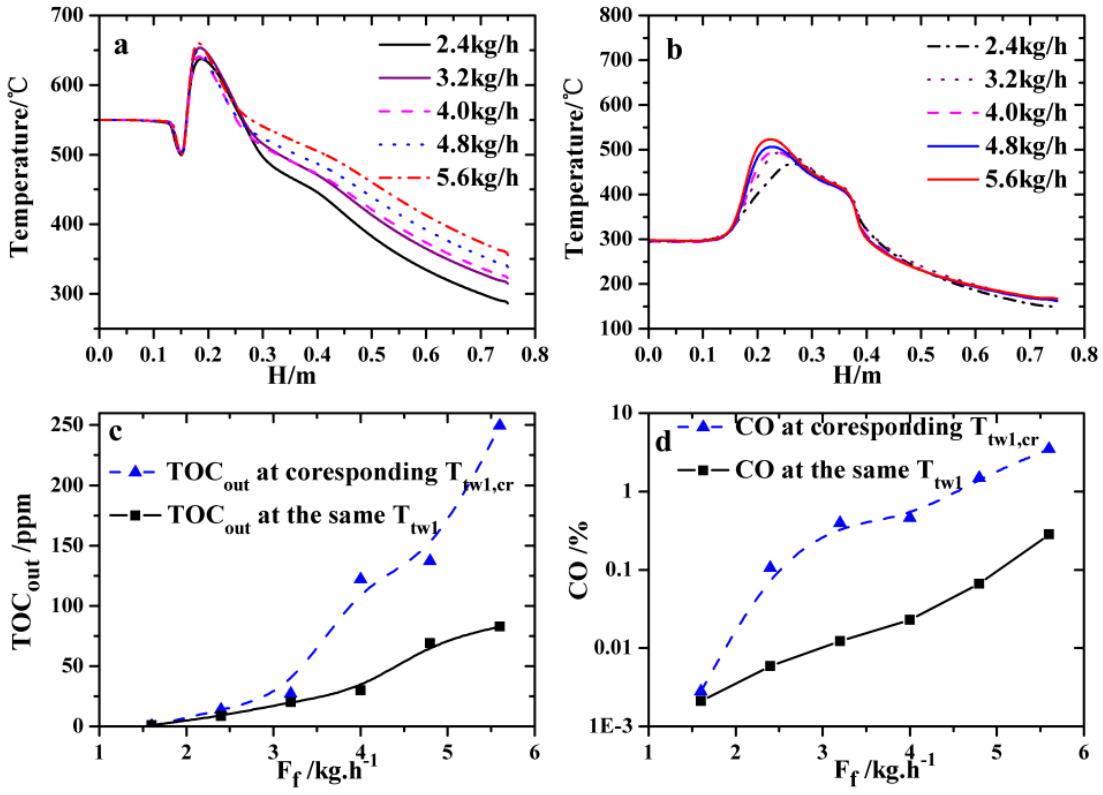

Fig. 11. The effect of feed flow on temperature profiles and product properties. (a) The axial temperature profiles along the reactor center, (b) the axial temperature profiles along the inner surface of the porous tube, (c) TOC_{out}, and (d) CO.

increased from 8.5 to 82.9 ppm and from 0.005% to 0.28%, respectively, when the feed flow was increased from 2.4 to 5.6 kg/h at the same T_{tw1}. However, feed degradation was further retarded at higher feed flows for lower $T_{tw1,cr}$. At the corresponding $T_{tw1,cr}$ for water film formation, TOC_{out} and CO were 13.9 ppm and 0.01%, respectively, when the feed flow was 1.6 kg/h. TOC_{out} and CO significantly increased to 249.4 ppm and 3.489%, respectively, when the feed flow was increased to 5.6 kg/h. Thus, the feed flow should be less than 4 kg/h to facilitate water film formation and feed degradation.

5. Conclusion

This study presented a CFD model of an inner preheating transpiring-wall reactor for SCWO oxidation. The reactor has been successfully operated in previous experiments. The numerical model was validated by comparing the experimental data and simulated results (such as temperature profiles, aqueous and gaseous products, etc.).

The eddy in the nozzle mixing zone and at the nozzle outlet indicated that the auxiliary heat source mixed with oxygen and the feed, respectively. Therefore, a continuously stirred tank reactor was probably formed in the upper part of the reactor for the intense mixing and the heat transfer. Meanwhile, a plug flow reactor was created in the lower parts of the reactor for the uniform velocity contours.

The transpiring flow relation exerted an insignificant effect on the temperature profiles, although T_{tw1} significantly influenced the temperature profiles inside the reactor. The inner surface temperature of the porous tube was critical to water film formation, and this temperature mainly depended on T_{tw1}. We defined $T_{tw1,cr}$ as the highest T_{tw1} that can maintain the porous tube's inner surface temperature below 374°C.

Increased feed concentration, feed flow rate, and F_f/F_{au} were found to be favorable for feed degradation at the same T_{tw1}. The $T_{tw1,cr}$ for the ideal water film formation was obtained by decreasing the temperature of tw1 step by step until the inner surface temperature of the porous wall was below 374°C. However, feed degradation was retarded at low $T_{tw1,cr}$. TOC_{out} and CO increased significantly when the feed concentration, feed flow rate, and F_f/F_{au} were increased at the corresponding $T_{tw1,cr}$ for water film formation.

The simulation results provided insight into the water film formation and product properties of the present inner preheating transpiring-wall reactor. Water film formation and feed degradation were mutually exclusive for the present reactor structural parameters. Thus, only a small processing capacity (lower feed flow, feed concentration, or F_f/F_{au}) can be allowed in this reactor. Nonetheless, the findings of this work can serve as guide for parallel works that will evaluate the effects of structural parameters on the reactor performance. Optimized structural parameters and operating parameters can be obtained by combining the findings of these works to establish the appropriate reactor design criteria.

Acknowledgments

This work is supported by National Natural Science Foundation (No. 51706049), Youth Innovation Promotion Association CAS (No. 2017412), PhD Start-Up Fund of Natural Science Foundation of Guangdong Province (No. 2014A030310203), Guangdong Province Science and Technology Plan Project (No. 2013B091100003; No. 2016B090918037), Nansha District technology development project (No. 2015KF013), Science research project of Guangzhou City (No. 201707010407, No. 201604010070), and Shenzhen Basic Research Project (No. JCYJ20150316144639927), China.

Symbols

a_c	—	Coefficient in Peng-Robinson equation
b_c	—	Coefficient in Peng-Robinson equation
C_p	—	Specific heat, J/kg K
CFD	—	Computational fluid dynamic
D	—	Mass diffusivity, m^2/s
E	—	Energy, J
E_f	—	Total fluid energy, J
E_s	—	Total solid medium energy, J
f	—	External body forces, N
F	—	Mass flow rate, kg/h
g	—	Acceleration due to gravity, 9.8 kg/s^2
G_b	—	Generation of turbulence kinetic energy due to buoyancy
G_k	—	Generation of turbulence kinetic energy due to the mean velocity gradients
H	—	Height, m
h_i^0	—	Enthalpy of formation of species i
h_j	—	Specific enthalpy of species j
I	—	Unit tensor
k	—	Turbulent kinetic energy
J	—	Diffusion flux, kg/m^2 s
k_{eff}	—	Effective thermal conductivity in the porous medium, W/m K
k_f	—	Thermal conductivity for the fluid phase, W/m K
k_s	—	Thermal conductivity for the solid medium, W/m K
L	—	Length, m
M	—	Molar mass, kg/mol
N_{sp}	—	Number of species
P	—	Pressure, Pa
r	—	Reaction rate; radius, m
R	—	Universal gas constant, 8.3145 kJ/mol
R_{tw}	—	Transpiring flow relation
S	—	Modulus of the rate of strain tensor
S_f^h	—	Fluid enthalpy source term
S_h	—	Sources of energy due to chemical reaction
S_i	—	ith the source term for porous media momentum equation
S_k, S_ε	—	User-defined source terms
SCWO	—	Supercritical water oxidation
t	—	Time, s
T	—	Temperature, °C
T_r	—	Reduced temperature
$T_{tw1,cr}$	—	Water film formation temperature, °C
TOC	—	Total organic carbon, ppm
u	—	Velocity vector, m/s
v	—	Molar volume, m^3/mol
x	—	Direction in space
Y	—	Species mass fraction

Y_M	—	Contribution of the fluctuating dilatation in compressible turbulence to the overall dissipation rate

Greek

α	—	Permeability, m^2
α_k	—	Inverse effective Prandtl numbers for k, $\alpha_k = 1.39$
α_ε	—	Inverse effective Prandtl numbers for ε, $\alpha_\varepsilon = 1.39$
β	—	Inertial resistance factor, m
γ	—	Stoichiometric oxygen excess
κ	—	Constant characteristic of component
ε	—	Turbulent dissipation
μ	—	Molecular viscosity, Pa s
ρ	—	Fluid density, kg/m
τ	—	Stress tensor, N
ϕ	—	Transpiring intensity
χ	—	Porosity of the medium
ω	—	Feed concentration, mass fraction, wt%
ψ	—	Acentric factor

Subscripts

au	—	Auxiliary heat source
C	—	Carbon
cr	—	Critical
f	—	Feed
ox	—	Oxygen
r	—	Reaction
sup	—	Supercritical
tw1	—	Upper branch of transpiring water
tw2	—	Middle branch of transpiring water

References

[1] N. Akiya, P.E. Savage, Roles of water for chemical reactions in high temperature water, Chem. Rev., 33 (2002) 2725–2750.

[2] Q. Wang, Y. Lv, R. Zhang, J. Bi, Treatment of cotton printing and dyeing wastewater by supercritical water oxidation, Desal. Wat. Treat., 51 (2013) 7025–7035.

[3] J.P.S. Queiroz, M.D. Bermejo, F. Mato, M.J. Cocero, Supercritical water oxidation with hydrothermal flame as internal heat source: efficient and clean energy production from waste, J. Supercrit. Fluids, 96 (2015) 103–113.

[4] V. Vadillo, M.B. Belén García-Jarana, J. Sánchez-Oneto, J.R. Portela, E.J.M. de la Ossa, Simulation of real wastewater supercritical water oxidation at high concentration on a pilot plant scale, Ind. Eng. Chem. Res., 50 (2011) 2512–2520.

[5] F.M. Zhang, S.Y. Chen, C.Y. Xu, G.F. Chen, C.Y. Ma, Energy consumption analysis of a transpiring-wall supercritical water oxidation pilot plant based on energy recovery, Desal. Wat. Treat., 51 (2013) 7341–7352.

[6] J.M. Zhang, C.Y. Ma, F.M. Zhang, G.F. Chen, Supercritical water oxidation of N-phenylglycinonitrile wastewater, Desal. Wat. Treat., 51 (2013) 3398–3407.

[7] M.D. Bermejo, M.J. Cocero, Supercritical water oxidation: a technical review, AIChE J., 52 (2006) 3933–3951.

[8] P.A. Marrone, Supercritical water oxidation-current status of full-scale commercial activity for waste destruction, J. Supercrit. Fluids, 79 (2013) 283–288.

[9] V. Vadillo, J. Sánchez-Oneto, J.R. Portela, E.J.M. de la Ossa, Problems in supercritical water oxidation process and proposed solutions, Ind. Eng. Chem. Res., 52 (2013) 7617–7629.

[10] M. Hodes, P.A. Marrone, G.T. Hong, K.A. Smith, J.W. Tester, Salt precipitation and scale control in supercritical water oxidation – part A: fundamentals and research, J. Supercrit. Fluids 29 (2004) 265–288.

[11] P. Kritzer, Corrosion in high-temperature and supercritical water and aqueous solutions: a review, J. Supercrit. Fluids, 29 (2004) 1–29.

[12] F.M. Zhang, S.Y. Chen, C.Y. Xu, G.F. Chen, J.M. Zhang, C.Y. Ma, Experimental study on the effects of operating parameters on the performance of a transpiring-wall supercritical water oxidation reactor, Desalination, 294 (2012) 60–66.

[13] D.H. Xu, S.Z. Wang, C.B. Huang, X.Y. Tang, Y. Guo, Transpiring wall reactor in supercritical water oxidation, Chem. Eng. Res. Des., 92 (2014) 2626–2639.

[14] K. Príkopský, B. Wellig, Ph. Rudolf von Rohr, SCWO of salt containing artificial wastewater using a transpiring-wall reactor: experimental results, J. Supercrit. Fluids, 40 (2007) 246–257.

[15] F.M. Zhang, S.Y. Chen, C.Y. Xu, G.F. Chen, C.Y. Ma, Research progress of supercritical water oxidation based on transpiring-wall reactor, Chem. Ind. Eng. Prog., 30 (2011) 1643–1650.

[16] C. Augustine, J.W. Tester, Hydrothermal flames: from phenomenological experimental demonstrations to quantitative understanding, J. Supercrit. Fluids, 47 (2009) 415–430.

[17] B. Wellig, K. Lieball, P. Rudolf Von Rohr, Operating characteristics of a transpiring-wall SCWO reactor with a hydrothermal flame as internal heat source, J. Supercrit. Fluids, 34 (2005) 35–50.

[18] M.D. Bermejo, P. Cabeza, J.P.S. Queiroz, C. Jiménez, M.J. Cocero, Analysis of the scale up of a transpiring wall reactor with a hydrothermal flame as a heat source for the supercritical water oxidation, J. Supercrit. Fluids, 56 (2011) 21–32.

[19] F.M. Zhang, Y. Zhang, C.Y. Xu, S.Y. Chen, G.F. Chen, C.Y. Ma, Experimental study on the ignition and extinction characteristics of the hydrothermal flame, Chem. Eng. Technol., 38 (2015) 2054–2066.

[20] F.M. Zhang, C.Y. Xu, Y. Zhang, S.Y. Chen, G. Chen, C.Y. Ma, Experimental study on the operating characteristics of an inner preheating transpiring wall reactor for supercritical water oxidation: temperature profiles and product properties, Energy, 66 (2014) 577–587.

[21] J. Abeln, M. Kluth, M. Böttcher, W. Sengpiel, Supercritical water oxidation (SCWO) using a transpiring wall reactor: CFD simulations and experimental results of ethanol oxidation, Environ. Eng. Sci., 21 (2004) 93–99.

[22] M.D. Bermejo, Á. Martín, J.P.S. Queiroz, I. Bielsa, V. Ríos, M.J. Cocero, Computational fluid dynamics simulation of a transpiring wall reactor for supercritical water oxidation, Chem. Eng. J., 158 (2010) 431–440.

[23] F.M. Zhang, C.Y. Ma, CFD simulation of a transpiring-wall SCWO reactor: formation and optimization of the water film, AICHE J., 62 (2016) 195–206.

[24] K. Lieball, Numerical Investigations on a Transpiring Wall Reactor for Supercritical Water Oxidation, PhD Thesis, ETH Zurich, Switzerland, 2003.

[25] D.H. Xu, C.B. Huang, S.Z. Wang, Y. Guo, Characteristics analysis of water film in transpiring wall reactor, Int. J. Heat Mass Transfer, 100 (2016) 559–565.

[26] S.A. Orszag, V. Yakhot, W.S. Flannery, F. Boysan, D. Choudhury, J. Maruzewski, B. Patel, Near-Wall Turbulent Flows, Elsevier Science Publishers, New York, 1993.

[27] S. Moussière, C. Joussot-Dubien, P. Guichardon, O. Boutin, H.A. Turc, A. Roubaud, B. Fournel, Modelling of heat transfer and hydrodynamic with two kinetics approaches during supercritical water oxidation process, J. Supercrit. Fluids, 43 (2007) 324–332.

[28] L. Li, P. Chen, E.F. Gloyna, Generalized kinetic model for wet oxidation of organic compounds, AIChE J., 37 (1991) 1687–1697.

[29] F. Vogel, J.L.D. Blanchard, P.A. Marrone, S.F. Rice, P.A. Webley, W.A. Peters, K.A. Smith, J.W. Tester, Critical review of kinetic data for the oxidation of methanol in supercritical water, J. Supercrit. Fluids, 34 (2005) 249–286.

[30] P. Dagaut, M. Cathonnet, J. Boettner, Chemical kinetic modeling of the supercritical-water oxidation of methanol, J. Supercrit. Fluids, 98 (1996) 33–42.

[31] J.W. Tester, P.A. Webley, H.R. Holgate, Revised global kinetic measurements of methanol oxidation in supercritical water, Ind. Eng. Chem. Res., 32 (1993) 236–239.
[32] C. Narayanan, C. Frouzakisa, K. Boulouchos, K. Príkopský, B. Wellig, P. Rudolf von Rohr, Numerical modelling of a supercritical water oxidation reactor containing a hydrothermal flame, J. Supercrit. Fluids, 46 (2008) 149–155.
[33] A. Leybros, A. Roubaud, P. Guichardon, O. Boutin, Supercritical water oxidation of ion exchange resins in a stirred reactor: numerical modeling, Chem. Eng. Sci., 69 (2012) 170–180.
[34] NIST, July 11, 2016. Available at: http://webbook.nist.gov/chemistry/fluid/
[35] E. Fauvel, C. Joussot-Dubien, V. Tanneur, S. Moussière, P. Guichardon, G. Charbit, F Charbit, A porous reactor for supercritical water oxidation: experimental results on salty compounds and corrosive solvents oxidation, Ind. Eng. Chem. Res., 44 (2005) 8968–8971.
[36] N. Zhou, A. Krishnan, F. Vogel, W.A. Peters, A computational model for supercritical water oxidation of organic toxic wastes, Adv. Environ. Res., 4 (2000) 75–90.
[37] S. Emerson, C. Stump, D. Wilbur, P. Quay, Accurate measurement of O_2, N_2, and Ar gases in water and the solubility of N_2, Mar. Chem., 64 (1999) 337–347.
[38] M.D. Bermejo, F. Fernandez-Polanco, M.J. Cocero, Modeling of a transpiring wall reactor for the supercritical water oxidation using simple flow patterns: comparison to experimental results, Ind. Eng. Chem. Res., 44 (2005) 3835–3845.

Supplementary information

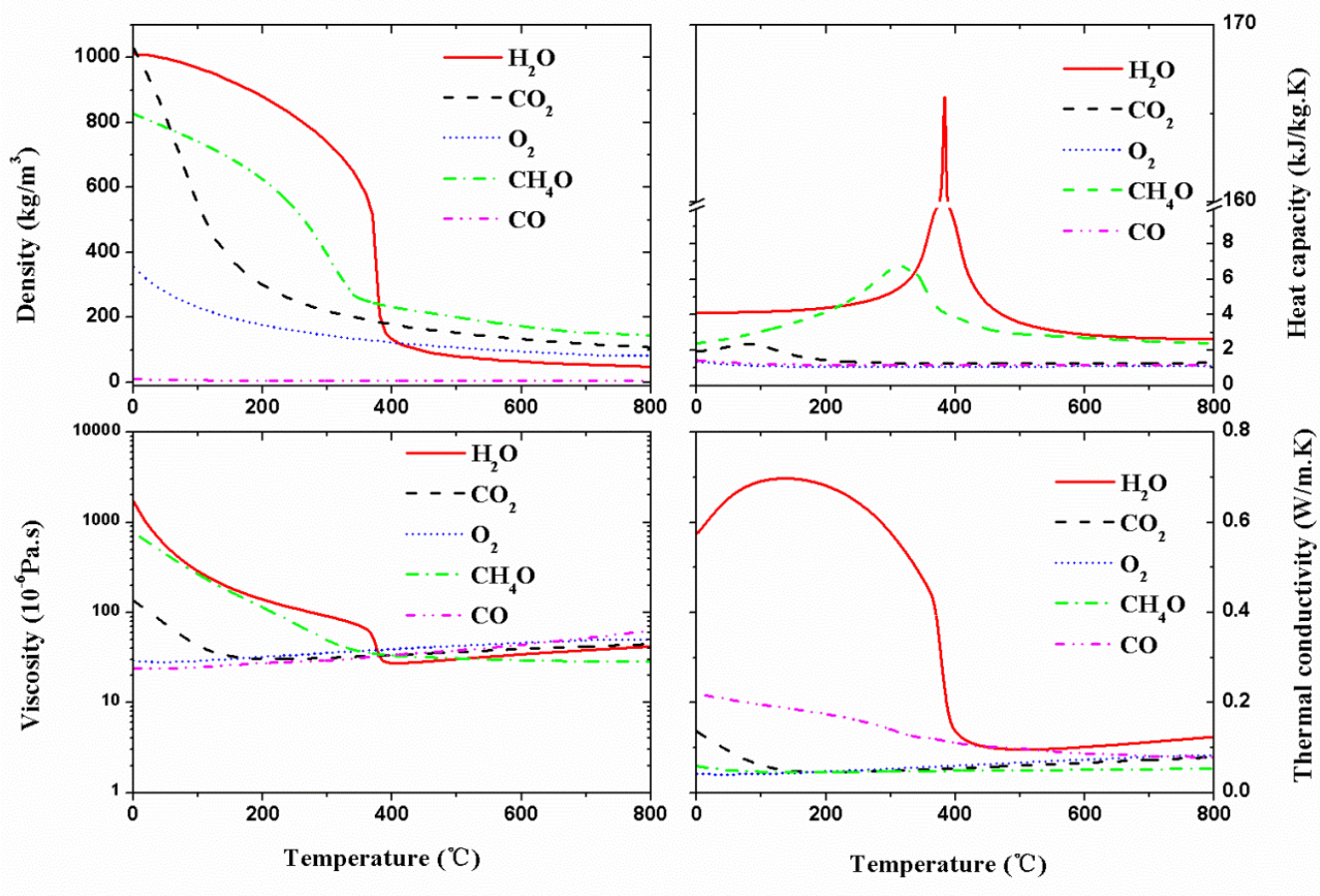

Fig. S1. Variation of component physical properties with temperature at 23 MPa.

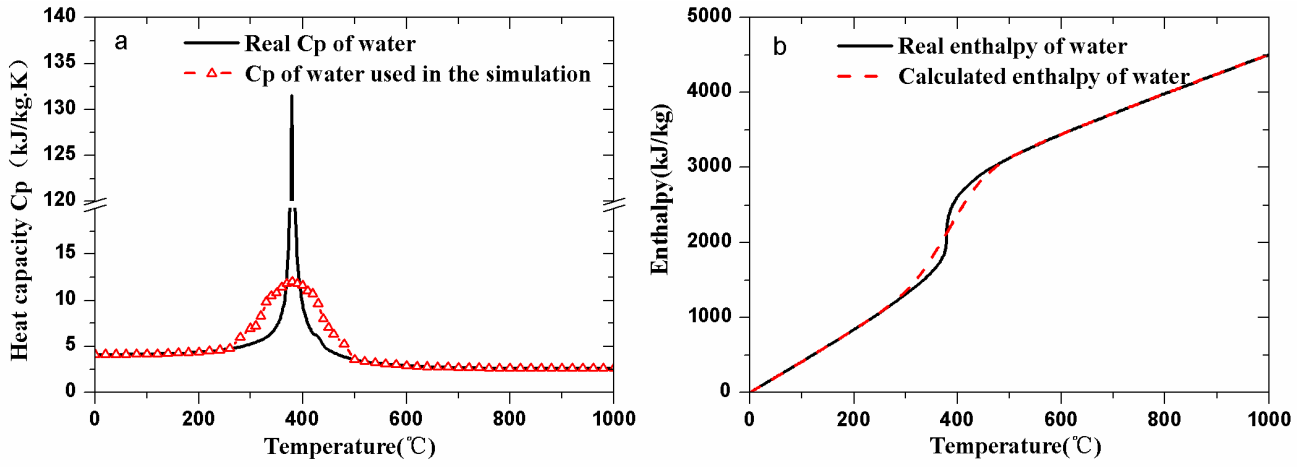

Fig. S2. The real C_p of water at 23 MPa and an approximation curve in the model.

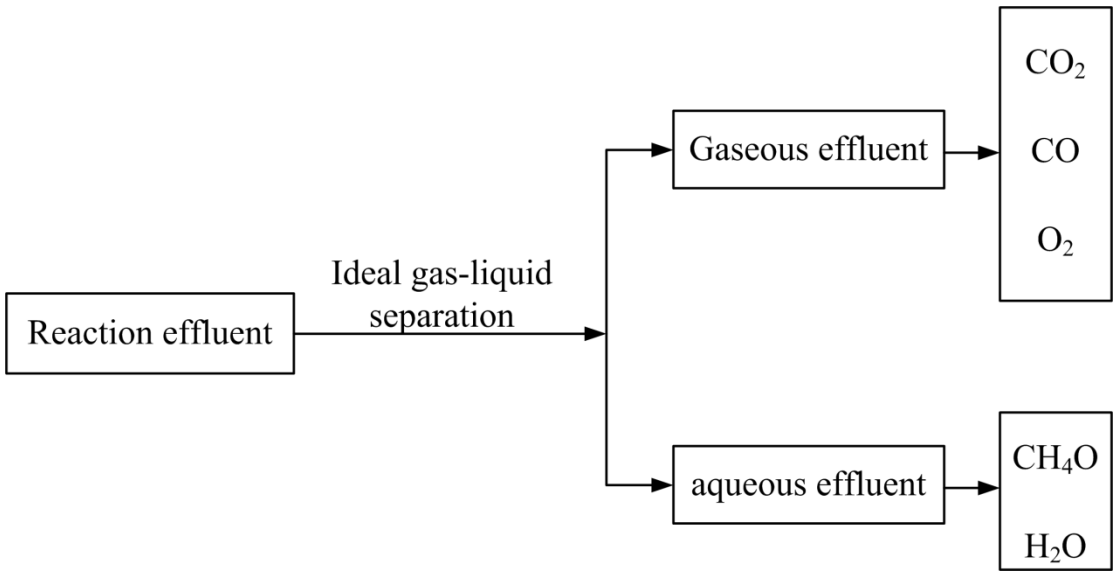

Fig. S3. An ideal gas–liquid separation of the reactor effluent in the simulation.

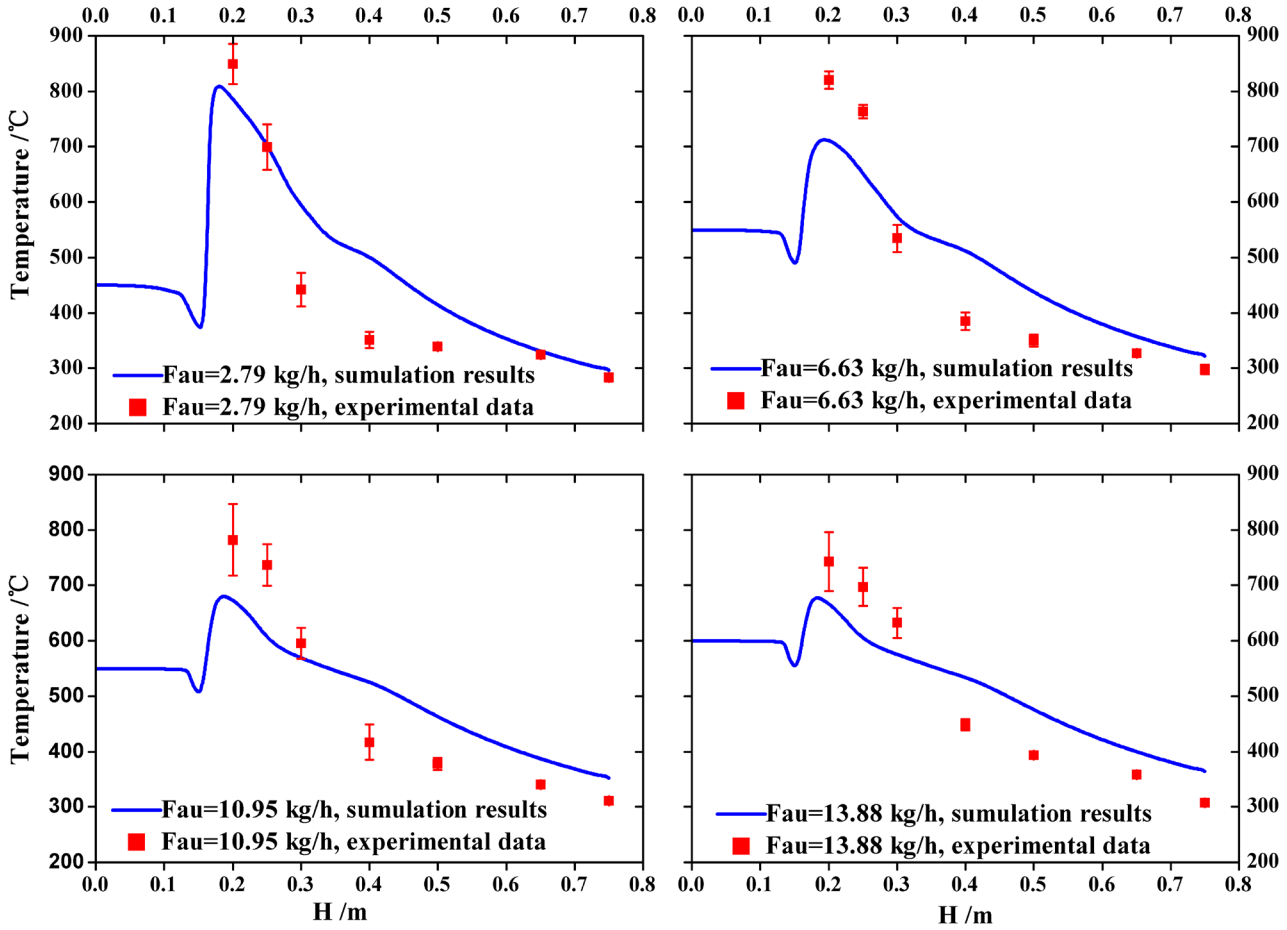

Fig. S4. Comparisons of the experimental and the calculated temperature profiles along the reactor axis at different auxiliary heat source flows, operating conditions: F_f = 3.5 kg/h, ω_f = 35 wt%, γ = 1.5, F_{tw1} = F_{tw2} = 19 kg/h, T_{au} = 550°C, and T_{tw1} = 350°C.

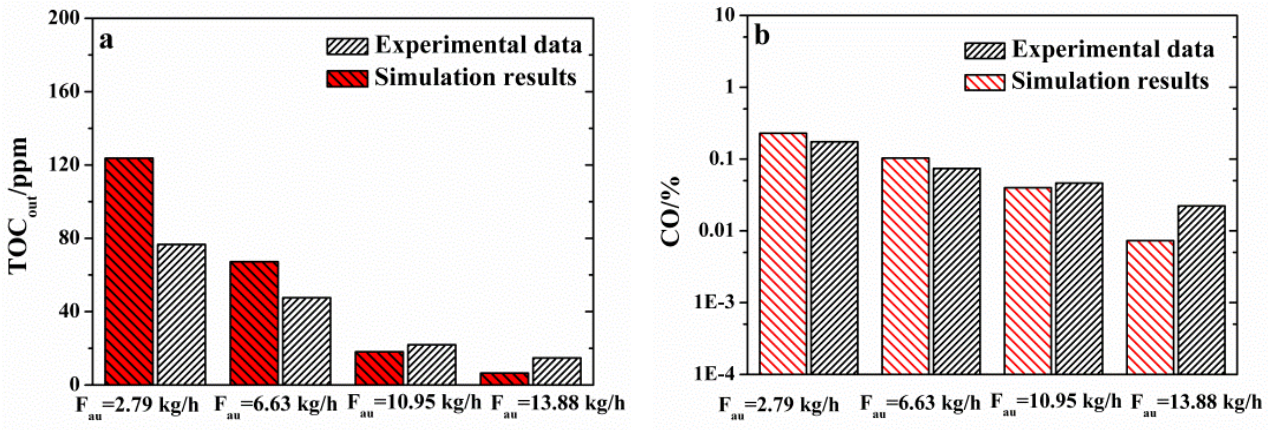

Fig. S5. Comparisons of the experimental and calculated concentrations of the effluent at different auxiliary heat source flows (a) TOC_{out} and (b) CO.

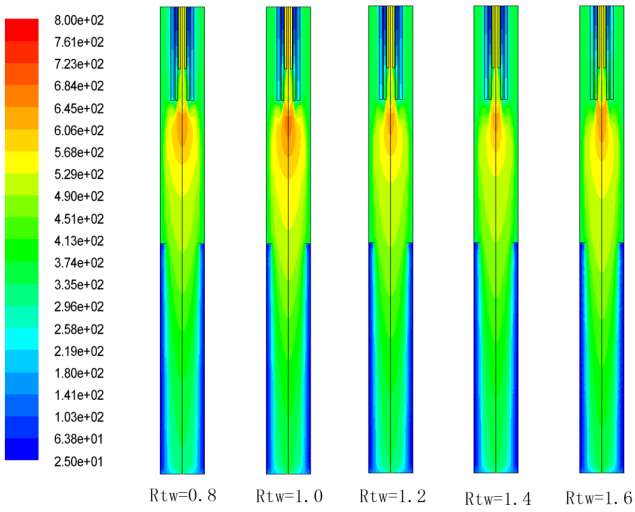

Fig. S6. Temperature contours at different transpiring flow relations.

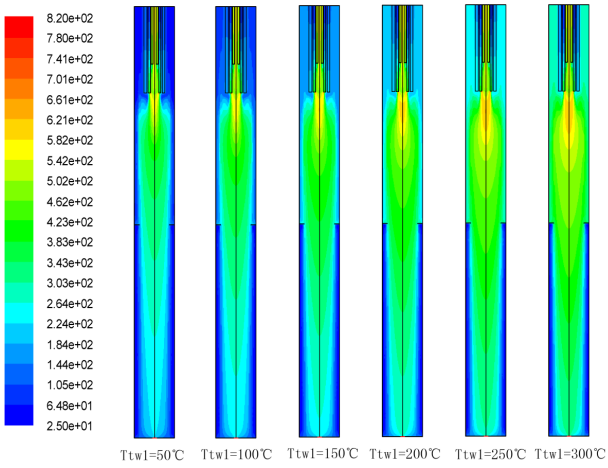

Fig. S7. Temperature contours at different transpiring water temperatures.